Group-velocity slowdown in a double quantum dot molecule

Stephan Michael,[1] Weng W. Chow,[2] and Hans Christian Schneider[1,*]

[1]*Department of Physics and Research Center OPTIMAS, University of Kaiserslautern, P.O. Box 3049, 67653 Kaiserslautern, Germany*

[2]*Semiconductor Materials and Device Sciences Department, Sandia National Laboratories, Albuquerque, New Mexico 87185-1086, USA*

(Received 24 June 2013; published 13 September 2013)

The slowdown of optical pulses due to quantum-coherence effects is investigated theoretically for an "active material" consisting of InGaAs-based double quantum dot molecules. These are designed to exhibit a long-lived coherence between two electronic levels, which is an essential part of a quantum-coherence scheme that makes use of electromagnetically induced transparency effects to achieve group-velocity slowdown. We apply a many-particle approach based on realistic semiconductor parameters that allows us to calculate the quantum dot material dynamics including microscopic carrier scattering and polarization dephasing dynamics. The group-velocity reduction is characterized in the frequency domain by a quasiequilibrium slowdown factor and in the time domain by the probe-pulse slowdown obtained from a calculation of the spatiotemporal material dynamics coupled to the propagating optical field. The group-velocity slowdown in the quantum dot molecule is shown to be substantially higher than what is achievable from similar transitions in typical InGaAs-based single quantum dots. The dependencies of slowdown and shape of the propagating probe pulses on lattice temperature and drive intensities are investigated.

DOI: 10.1103/PhysRevB.88.125305 PACS number(s): 78.67.Hc, 42.50.Gy

I. INTRODUCTION

Quantum-coherence effects encompass a variety of interference effects in the coherences, i.e., transition amplitudes, between quantum states that are driven by laser light. In quantum optics, they have been known for decades.[1–6] In particular, electromagnetically induced transparency (EIT) is based on the quantum interference associated with a long-lived coherence, which can make an optically thick medium transparent for a probe field in the presence of a drive field. Because the coherent effects also modify the dispersive properties, a very small group velocity may occur for pulses, which is usually referred to as slow light. Electromagnetically induced transparency, group-velocity slowdown, and other quantum-coherence effects have been intensively investigated in atomic, molecular, and optical (AMO) physics; see, e.g., Refs. 1 and 7. There have been different proposals to realize quantum-coherence effects in few-level systems in solid state[8–15] and especially semiconductors[8,10,11,16–21] because of the possible importance of these effects for optical information processing, such as an optical delay line. Slow light has been achieved in semiconductor quantum wells using setups that employ coherent population oscillations of excitons instead of the EIT-type processes in quantum dots (QDs) considered in the present paper.[12,22] Other approaches, for instance, involving slow light in photonic crystals, are also being actively pursued.[23]

Semiconductor QDs, which are arguably the closest realization of a system with localized states and discrete energies in semiconductors, are a natural candidate for the realization of quantum-coherence processes[24–28] in a material for which extremely advanced growth and processing techniques exist. However, for electron-hole transitions in semiconductors typical dephasing times severely limit the achievable group-velocity slowdown, even in QDs,[28,29] where there is the smallest "phase space" for scattering and dephasing processes. As it is known from quantum optics, such a pronounced dephasing is detrimental for quantum-coherence effects. Depending on the levels that are connected by drive and probe fields, Λ, V and ladder schemes can be realized, and these can be compared directly as long as one applies an AMO model that assumes dephasing constants for the various polarizations involved in the respective schemes.[28] For instance, it has been shown that the structural QD parameters can generally be more easily optimized for V schemes than for other schemes.[27,30]

We discuss in this paper only V-type schemes, as opposed to the Λ schemes analyzed earlier by us,[25,31,32] in which the quantum coherence connected two hole states. In such a Λ setup there is a sizable dephasing of the quantum coherence from the hole states because they are closely spaced and broadened by polaronic interaction effects. This problem can partly be circumvented by using a short drive pulse,[31,32] but the time window, during which the probe pulse is slowed down, is too short to be useful for applications.[33]

In this paper we make a theoretical proposal for a QD *molecule* that is designed to lead to a long-lived coherence between its lowest electronic levels. The proposed design consists of two QDs of different sizes stacked in growth direction, and should be within reach of current fabrication techniques, as evidenced by recent investigations that have shown how QD molecules can be fabricated with prescribed properties.[34–36] The lineup of the energy levels of the proposed QD molecule are not qualitatively different from those of a single InGaAs-based QD, for which quantum-coherence effects have already been investigated.[25,30–32] What sets the molecule apart from the single QD is the "wave-function engineering" that leads to dipole matrix elements and dephasing rates that are favorable for group-velocity slowdown. We demonstrate this by employing a model from semiconductor many-particle physics rather than an AMO model. We stress that, while an AMO model uses constant dephasing rates for the individual levels and the dipole matrix elements as input, our approach uses the relevant matrix elements from a simplified QD electronic structure calculation and computes, in a microscopic fashion, the dephasing and scattering processes in QD molecules due to the Coulomb interaction between

charged carriers and/or the carrier-phonon interaction. Based on this approach, we characterize the slowdown factor of these QD molecules in the frequency domain and explicitly calculate the group-velocity slowdown of a probe pulse propagating in a semiconductor host surrounding these model QD molecules. For the dynamical calculation, we combine a determination of the propagating optical fields, as in Refs. 28 and 29, with a microscopic theory for the calculation of scattering and dephasing processes along the lines of Refs. 37–42. Work in this area has recently been comprehensively reviewed in Ref. 43.

The paper is organized as follows. The design of the asymmetric QD molecule is presented along with a calculation of its electronic single-particle states and energies in Sec. II. Results from the semiconductor Bloch equations including many-particle scattering and dephasing effects as they apply to QDs and from the treatment of pulse propagation in semiconductors are gathered in Sec. III. Using the semiconductor Bloch equations, we first investigate the slowdown factor and the slowdown-bandwidth product determined from the spectral features for different lattice temperatures and cw drive intensities in Sec. IV A. Next, in Sec. IV B we determine the slowdown factor and pulse characteristics directly from the propagating probe field. We investigate the influence of the probe-pulse shapes for different lattice temperatures, and cw drive intensities. We compare these results with the group-velocity slowdown determined from the spectral features. The final discussion of Sec. V concerns the differences to quantum-coherence schemes in single semiconductor QDs. The setup for the single QDs including electronic single-particle states and energies is presented in Sec. V A. The slowdown factor determined from the spectral features for different lattice temperatures and cw drive intensities is investigated in Sec. V B. These results are compared to the QD molecule results from Sec. IV A in Sec. V C. We present our conclusions in Sec. VI.

II. ELECTRONIC STRUCTURE OF THE QD MOLECULE

The purpose of this section is to introduce the design of an asymmetric QD molecule with an electronic structure that is particularly well suited for quantum-coherence effects in a V configuration. We do not aim at a comprehensive theory of the electronic structure of QD molecules, which would have to include the complicated alloy concentration and strain fields of the QD molecule and the surrounding structure. Rather, we describe here a numerically tractable model that includes the geometry of the QD *molecules* under study as well as static electric fields and works with a few meaningful parameters that characterize the structure. In particular, we compute the single-particle states, i.e., wave functions and energies of the double QD molecules from the states of the two underlying single QDs that make up the molecule. In the following, we assume that the QD molecules are formed from two vertically stacked QDs, separated by a spacer layer, such as one of the three double layers sketched in Fig. 1. We assume that the QD molecules are embedded in a quantum well and take the QW continuum states as plane waves that are orthogonalized to the localized states of the QD molecule; see Ref. 44.

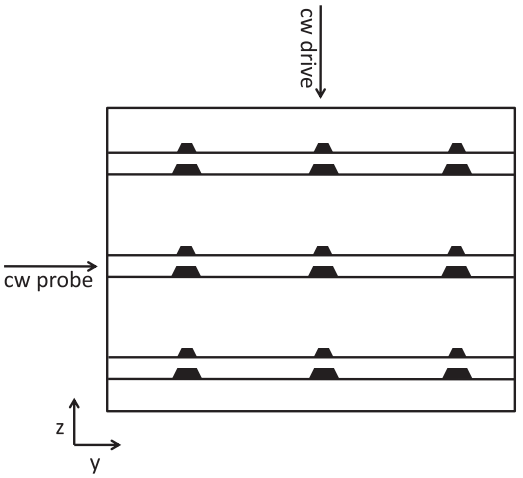

FIG. 1. Schematic drawing of setup for the calculation of group-velocity slowdown with a V scheme formed by levels in the QD molecules as shown in Fig. 2. For the determination of the slowdown factor, the drive field is assumed to be cw; for the dynamical calculation a "quasi-cw" drive pulse with duration much larger than the probe pulse is used.

For the QDs we assume that they are grown on a wetting layer embedded in a quantum well. We use the envelope-function approximation and assume a cylindrical confinement potential of finite depth which yields semianalytical results for the wave functions and energies. This approach is described in detail in Appendix A 1. We stress that, although no strain, piezoelectric effects, or structural anisotropies are included in the single QD model, its parameters are adjusted to more accurate $k \cdot p$ QD calculations[45,46] with material parameters as used in Ref. 32.

We start with the description of the two separate QDs that will be combined to the double-QD molecule. Since the QD molecule should be asymmetric, we identify the single QDs as the "small" and the "large" one. For the small QD, we assume an $In_{0.8}Ga_{0.2}As$ QD embedded in a GaAs quantum well on a wetting layer of thickness 1 nm. The QD has a diameter of 10 nm and a height of 2 nm. For this QD geometry only the lowest electron and hole states are confined. For the large QD, we assume an $In_{0.9}Ga_{0.1}As$ QD embedded in a GaAs quantum well on a wetting layer of thickness 1 nm. The cylindrical QD model has a diameter of 12 nm and a height of 3 nm. For this structure three electron and three hole states are confined. The different sized QDs have different energy spacings between the levels. In particular, no energetic degeneracies between levels of the small and the large QD occurs.

The states of the two cylindrical QDs described above are the limiting case for a level structure of a QD molecule composed of the individual QDs, but with a very large spatial separation between the two. When the QDs are closer together with a potential barrier between them, the levels of the original QDs are mixed to form the single-particle states of the QD molecule. The states of the QD molecule are obtained from a linear combination of the orbitals of the QDs, as described in Appendix A 2. In this approach, the effect of external static electric fields is also included. The QD molecule is designed by choosing a combination of an external field in growth direction and a separation of the QDs, so that the lowest hole levels of

TABLE I. Electron (e) and hole (h) energies of single-particle states in the QD molecules. The bonding and antibonding states formed from hole levels of the individual QDs are denoted by h^b and h^a, respectively.

State	E_e (meV)	State	E_h (meV)
e_0	−194	h_0^b	55
e_1	−132	h_1^a	47
$e_{2/3}$	−56	$h_{2/3}$	13

the two QDs are lined up without bringing the QDs too close to together. We choose a static electric field in growth direction of $E_\perp = 1.5$ mV/nm and a QD distance of 14 nm, placing the QD molecule in the center of a 30-nm surrounding quantum well. For the QD molecule we obtain four confined hole and electron states whose energies are compiled in Table I. The lineup of the levels is shown schematically together with a sketch of the most important wave functions in Fig. 2. There is only a very small overlap between wave functions of the lowest electronic levels $e_{0/1}$, which are only very weakly mixed states that are mainly localized in the individual QDs. The lowest QD hole levels, however, are bonding h_0^b and antibonding h_1^a states formed from the lowest hole levels in the individual QDs. Further, the transitions between the lowest bonding hole level h_0^b and the electron levels e_0 and e_1 are dipole allowed with dipole moments of $0.5e$ nm and $0.2e$ nm, respectively.

The design of the QD molecule thus leads to a level structure and dipole moments that are especially well suited for a V-configuration with probe and drive fields connecting the $h_0^b \leftrightarrow e_1$ and $h_0^b \leftrightarrow e_0$ states as shown in Fig. 2. Quantum-coherence effects in the V scheme are particularly pronounced if the transition $e_0 \leftrightarrow e_1$ is long lived, i.e., exhibits only a small polarization dephasing. This is the transition that is

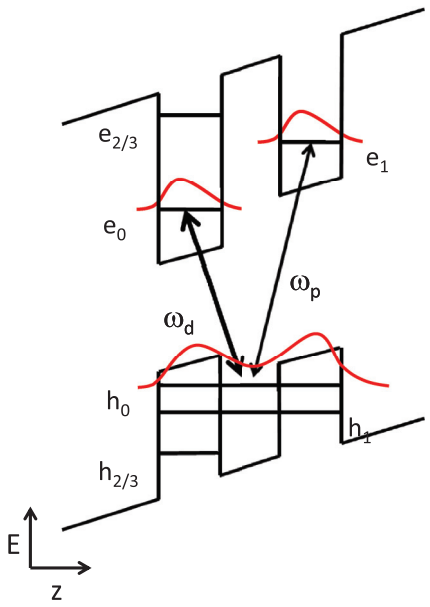

FIG. 2. (Color online) Schematic picture of the lowest-level wave functions and the geometry of the asymmetric double-QD molecule described in the text. The resonant probe and drive fields in a V-type quantum-coherence scheme are also shown.

"engineered" to connect electronic states of the QD molecule that are more or less localized in the different individual QDs and therefore have a very small wave-function overlap. We refer to the accompanying polarization as the *quantum coherence*.

III. SEMICONDUCTOR MAXWELL-BLOCH EQUATIONS

In this section, we summarize the equations for the propagating optical fields and the coupling to the semiconductor Bloch equations, which are used to describe the V scheme of the QD system. The propagating optical field is written in the form

$$\vec{E}(y,t) = \tfrac{1}{2}\hat{x}[\mathcal{E}(y,t)e^{i(ky-\omega t)} + \mathcal{E}(y,t)e^{-i(ky-\omega t)}], \quad (1)$$

where the propagation is in the y direction, $\hat{x}$ is the polarization unit vector in the x direction, k is the wave vector, and ω is the frequency of the field $\vec{E}$. The corresponding macroscopic polarization has the form

$$\vec{P}(y,t) = \tfrac{1}{2}\hat{x}[\mathcal{P}(y,t)e^{i(ky-\omega t)} + \mathcal{P}^*(y,t)e^{-i(ky-\omega t)}], \quad (2)$$

where $\mathcal{P}$ is the complex slowly varying envelope. Substituting these forms into the wave equation and employing the slowly varying envelope approximation, one obtains the slowly varying Maxwell equations.[47,48] The substitution $t' = t - n_b y/c$, where n_b is the background refractive index, transforms the partial differential equation into an ordinary differential equation with respect to the scaled spatial variable y,

$$\frac{\partial}{\partial y}\mathcal{E} = i\frac{n_b\omega}{2\varepsilon c}\mathcal{P}. \quad (3)$$

This equation neglects the dependence on the transverse and lateral coordinate of the fields. We assume in the following that the lateral and transverse extension of the probe pulse, which is propagated by Eq. (3) in our setup (see Fig. 1) is such that this approximation is fulfilled.

The macroscopic polarization P is connected with the microscopic polarization by

$$P = \frac{N_d}{L}\sum_{\alpha,\beta}\mu_{\alpha\beta}p_{\alpha\beta} + \text{c.c.}, \quad (4)$$

where N_d is the density of QDs in the quantum well layer, L is the thickness of the quantum well, in which the QDs are embedded, $\mu_{\alpha\beta}$ are the dipole matrix elements, and the summation index α or β refers to QD system electron or hole states, respectively.

A. Semiconductor Bloch equations

The dynamics of the polarizations and carrier distributions at the single-particle level are calculated in the framework of the semiconductor Bloch equations for the reduced single-particle density matrix. We denote in the following electron and hole levels in the QD α and β, respectively. For the V system of interest in this paper one obtains the following equations of motion for the "interband" polarizations, $p_{\alpha\beta}$,

and the "intra(electron-)band" polarizations $p_{\alpha'\alpha''}$:

$$\frac{\partial}{\partial t}p_{\beta\alpha} = -i\omega_{\alpha\beta}p_{\beta\alpha} - i\Omega_{\alpha\beta}\left(n^c_\alpha - n^v_\beta\right) - i\sum_{\alpha'\neq\alpha}\Omega_{\alpha'\beta}p_{\alpha'\alpha} + S_{\beta\alpha}, \quad (5)$$

$$\frac{\partial}{\partial t}p_{\alpha'\alpha''} = -i\omega_{\alpha''\alpha'}p_{\alpha'\alpha''} - i\Omega_{\alpha''\alpha'}\left(n^c_{\alpha''} - n^c_{\alpha'}\right) + i\sum_{\beta'}(\Omega_{\alpha''\beta'}p_{\alpha'\beta'} - \Omega_{\beta'\alpha'}p_{\beta'\alpha''}) + S_{\alpha'\alpha''}. \quad (6)$$

In particular, the polarization $p_{e_0e_1}$ here is the *quantum coherence*. For the time evolution of the conduction and valence band populations, n^c_α and n^v_β, one obtains

$$\frac{\partial}{\partial t}n^c_\alpha = i\sum_{\beta'}(\Omega_{\alpha\beta'}p_{\alpha\beta'} - \Omega_{\beta'\alpha}p_{\beta'\alpha}) + S_{\alpha\alpha}, \quad (7)$$

$$\frac{\partial}{\partial t}n^v_\beta = i\sum_{\alpha'}(\Omega_{\beta\alpha'}p_{\beta\alpha'} - \Omega_{\alpha'\beta}p_{\alpha'\beta}) + S_{\beta\beta}. \quad (8)$$

The coherent contributions of the above equations contain transition frequencies $\omega_{\alpha\beta}$ and renormalized Rabi frequencies $\Omega_{\alpha\beta} = \hbar^{-1}\mu_{\alpha\beta}E(t) + \Omega^{\mathrm{HF}}_{\alpha\beta}$. Here, $E(t)$ is the electric field at the position of the QD and the excitation-dependent Hartree-Fock (HF) contributions Ω_{HF} result from the Coulomb interaction, as discussed, e.g., in Refs. 25,31, and 32.

The correlation contributions are generally denoted by S and contain the influence of electron-electron and electron-phonon interactions beyond the Hartree-Fock level. In particular, $S_{\alpha,\alpha}$ and $S_{\beta,\beta}$ describe scattering contributions in the dynamical equations for the electron and hole distributions as well as dephasing $S_{\beta\alpha}$, $S_{\alpha'\alpha''}$ in the dynamical equations for the coherences.

B. Scattering/dephasing contributions

Dephasing processes are extremely important for the description of pulse slowdown in semiconductors. From quantum optics it is well known that the dephasing rate of the quantum coherence has a decisive influence on the behavior of quantum-coherence schemes. In fact, the engineering of the QD molecule was done with the goal of realizing a comparatively small dephasing rate for the quantum coherence between the e_0 and e_1 levels. For short-pulse dynamics, also the population dynamics play a role, and we therefore have to examine both dephasing and scattering contributions to the semiconductor-Bloch equations as they apply to our proposed QD molecule. Scattering processes in the QDs connect discrete levels so that the influence of level broadening is much more pronounced than for scattering between continuum states in quantum wells.

We are here concerned with a treatment of carrier relaxation and polarization dephasing that captures the essential features for the analysis of our quantum-coherence scheme. To begin with, the broadening of QD levels is mainly provided by the interaction of electrons with phonons and with other electrons in the scattering continuum, which we assume to be formed in the quantum well embedding the QDs. We are only concerned with excitation conditions in which the continuum states are not appreciably populated by carriers. In this case of vanishing excitation of the continuum states, the electron-phonon interaction has been shown to dominate over the electron-electron interaction for scattering processes and dephasing processes that can be associated with real scattering transitions (as opposed to "pure-dephasing" processes). We therefore consistently neglect electron-electron interactions for both of these processes and describe first our treatment of the electron-phonon interaction.

Since the broadening of the discrete levels is important for QDs, it is more appropriate to work with polarons, i.e., quasiparticles that include the effect of the coupling to phonons, instead of the "naked" QD electronic levels. Qualitatively, the polaron spectrum contains a peak at the "naked" electron energy as well as sidebands due to coupling to the discrete LO phonons. Coupling to a continuum, such as acoustic phonons, adds an additional broadening to the peak and the sidebands. In this case, the relaxation and dephasing contributions for the carrier distributions and polarizations cannot easily be computed using Fermi's Golden Rule arguments because there is no straightforward energy conservation for transitions between polarons. Instead, we follow Refs. 38–40 and obtain the scattering and dephasing contributions from the Keldysh Green's function technique. In particular, we employ the random-phase approximation (RPA) for the electron-phonon interaction contributions to the electron, or rather, polaron self-energy.

Our treatment of scattering and dephasing contributions is described in Appendix B; here we only summarize our approach. As shown in Ref. 39, the full polaronic dynamics is, in principle, not determined by equations of the form (5)–(8), but rather by coupled equations of motion for "spectral" and "kinetic" Green's functions *depending on two time arguments* whose numerical solution is extremely demanding. We therefore follow the spirit of Ref. 40 and separate the spectral properties of the polarons in order to get equations of motion for the dynamical distributions and polarizations as defined above. This procedure yields scattering and dephasing contributions of the form appearing in Eqs. (5)–(8) that still include memory integrals with information about the polaronic spectrum.

In contrast to Ref. 40, we use a Markov approximation and introduce an *effective quasiparticle broadening* in the memory integrals. This finally yields the scattering and dephasing contributions as employed in the following calculations. The explicit expressions are given in Appendix B and contain the effect of the electron-phonon interaction on the polaronic spectrum in the form of complex renormalized energies of a single-particle QD state λ,

$$\tilde{\epsilon}_\lambda = \epsilon_\lambda + \Delta\epsilon_\lambda - i\Gamma_\lambda, \quad (9)$$

where $\Delta\epsilon$ contains the real Hartree-Fock energy shift and a small correlation contribution. The broadening Γ_λ of the level λ is entirely due to correlations. We use in the following a constant level broadening $\Gamma = 0.84\ \mathrm{ps}^{-1}$ for a lattice temperature of $T_L = 300$ K and $\Gamma = 0.50\ \mathrm{ps}^{-1}$ for $T_L = 150$ K, respectively.[33] Although the precise value of Γ does not affect the numerical results for our quantum-coherence scheme, it is important to get its order of magnitude right, and we have determined these numerical values from single-pole approximations to the zero-density QD polaronic spectral functions, computed as in Refs. 38,40, and 49.

As mentioned above, we neglect the Coulomb-interaction contribution to scattering and dephasing processes that involve

continuum states. However, there are pure-dephasing contributions from the Coulomb interaction between carrier states in the QD, most notably processes in which two electrons effectively exchange their single-particle states. We therefore take the Coulomb interaction between states *in the QD* into account, because the electron-phonon contribution to the dephasing of the quantum coherence can be very inefficient, especially for deep QDs, in which the energy conservation between the widely spaced electronic levels and a LO phonon cannot be fulfilled, even including the polaronic broadening. As in the case of the carrier-phonon interaction, we follow Refs. 40 and 41 for the treatment of the Coulomb interaction contribution and employ the self-energy in second-order Born approximation along with the Markov approximation in the scattering kernels, as well as a single-pole approximation for the polaronic spectral properties. Because the continuum states are not appreciably populated by carriers we neglect, in contrast to Ref. 40, the Coulomb-interaction contribution to the *effective quasiparticle broadening*. The relevant equations, including a statically screened Coulomb potential, have the structure as shown in Appendix B.

IV. NUMERICAL RESULTS FOR THE QD MOLECULE

In this section we present numerical results with the eventual aim to characterize the slowdown achievable in a structure composed of a single layer of double QD molecules for the geometry shown in Fig. 1. We assume a strong cw drive field in the z direction and a weak cw or probe field in the y direction. As we do not include propagation effects for the drive field, our results also apply to multilayer QD molecule structures, as already indicated in Fig. 1 as long as the layers are stacked tightly enough in the z direction that propagation effects are unimportant and if the propagating field is guided such that it overlaps well with the QD active material.

Because of the drive-field-induced energy shifts of the sharp and closely spaced resonances, it is advantageous to first neglect propagation effects for the probe field and analyze the spectral properties experienced by a weak cw probe field in Sec. IV A. Although the measure of the achievable slowdown that can be obtained from the spectra is not as accurate as the slowdown for propagating probe pulses computed in Sec. IV B, the spectra yield important information on the width of the spectral region in which slowdown is possible and also on the magnitude of the slowdown when studying the influence of parameters, such as drive intensity or temperature. Further, the spectral information is necessary to properly tune the probe pulse in order to maximize the slowdown.

A. Spectra and slowdown factor

We first investigate the spectral features of the slowdown factor and the spectral width over which slowdown can be achieved. To this end, we solve the dynamical equations (5)–(8) for a strong cw drive field with fixed angular frequency ω_d and a weak cw probe field with angular frequency ω_p. From the steady-state value of the polarization $\mathcal{P}$ we determine the gain via

$$g(\omega_p) = -\frac{\omega_p}{2\varepsilon_0 c n_b \mathcal{E}_p}\mathrm{Im}[\mathcal{P}] \tag{10}$$

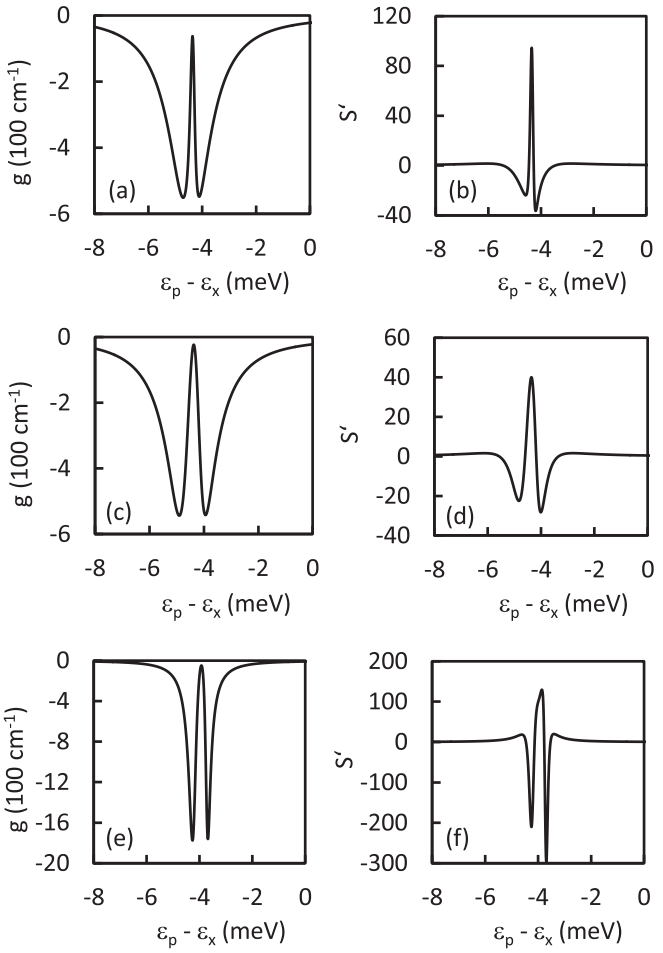

FIG. 3. Gain g and slowdown S' versus probe detuning for $T = 300$ K, $I_d = 0.25$ MW/cm^2 (a),(b); $T = 300$ K, $I_d = 0.7$ MW/cm^2 (c),(d); and $T = 150$ K, $I_d = 0.25$ MW/cm^2 (e),(f). The unexcited exciton transition energy is denoted by ϵ_x.

and refractive-index change

$$\delta n(\omega_p) = -\frac{1}{2\varepsilon_0 n_b \mathcal{E}_p}\mathrm{Re}[\mathcal{P}], \tag{11}$$

where n_b is the background refractive index of the host material. The group-velocity slowdown factor is defined by $S(\omega_p) = n_b + \omega_p \frac{d(\delta n)}{d\omega_p} \equiv n_b + S'(\omega_p)$, but we consider only the contribution from the index change,

$$S'(\omega_p) = \omega_p \frac{d\,(\delta n)}{d\omega_p}, \tag{12}$$

in order to remove the static contribution, which describes the change in group velocity due to the background refractive index as compared to vacuum. For the numerical calculations we assume a lattice temperature of $T = 300$ K and a cw probe with a field intensity of $I_p = 45$ W/cm^2. For a cw drive intensity of $I_d = 0.25$ MW/cm^2 we obtain the spectra shown in Figs. 3(a) and 3(b) and for a cw drive intensity of $I_d = 0.7$ MW/cm^2 we obtain the ones shown in Figs. 3(c) and 3(d). Before discussing these spectra in some detail, we emphasize that the width of the spectral features in Fig. 3 is *not* due to effective dephasing rates for the different polarizations in the system. Instead, the spectral location and the width

of the features is entirely due to the calculated dephasing (and scattering) contributions, which are determined by the electronic structure of the QD molecule and the excitation conditions. Nevertheless, one can attempt to extract effective dephasing rates for three-level systems for specified excitation conditions. We defer this question to the end of Sec. IV B.

The HF corrections lead to renormalizations of the transition frequencies as well as of the generalized Rabi frequencies when the excitation, i.e., the drive intensity, is increased. In particular, excitation-dependent HF energy corrections lead to an energy shift of approximately 4.2 meV in Figs. 3(a)–3(d). Also a small asymmetry, more pronounced for the slowdown factor and less pronounced for the gain, occurs due to the influence of the HF corrections.

Figures 3(a)–3(d) show the typical signatures of EIT[1,50]: a dip in the absorption profile and an increase of the slowdown factor S' at the dip. For the sake of simplicity, we refer to the existence of two transitions, which are "dressed" by the strong coherent drive field, as Autler-Townes splitting. This splitting is proportional to the drive intensity. The EIT signatures are due to an additional quantum interference effect between the Autler-Townes resonances. It is particularly important for the existence of EIT that the dephasing rate of the quantum coherence γ_{nr} be much smaller than the dephasing rate of the polarization γ_{probe}. An increased drive intensity of $I_{\mathrm{d}} = 0.7\ \mathrm{MW/cm^2}$ leads to a larger separation of the Autler-Townes resonances and a reduction of the peak slowdown factor S'; see Figs. 3(c) and 3(d). Also, an additional excitation-induced broadening of the spectral features for higher drive intensities occurs because the dephasing contributions depend on the level occupations and the polarizations, so that the dephasing of a particular transition depends on the drive pulse.

Keeping the drive intensity at $I_{\mathrm{d}} = 0.25\ \mathrm{MW/cm^2}$, but reducing the temperature to 150 K, leads to weaker dephasing and thus a more pronounced effect of the quantum interference, i.e., a more pronounced dip in Fig. 3(e) and higher peak slowdown in Fig. 3(f) compared with Figs. 3(a) and 3(b), respectively. Due to the different occupation of the states for lower temperatures the HF shift of the probe transition energy is around 3.9 meV for 150 K, instead of 4.2 meV for 300 K. Also the asymmetry of the spectra induced by HF corrections is more pronounced for lower temperatures.

The dependence on the drive intensity for the gain and the peak slowdown is shown in Fig. 4 for lattice temperatures of

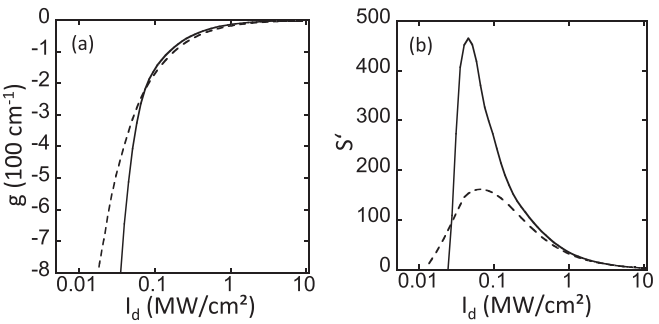

FIG. 4. Peak gain (a) and peak slowdown (b) versus drive intensity for a lattice temperature of 300 K (dashed line) and 150 K (solid line).

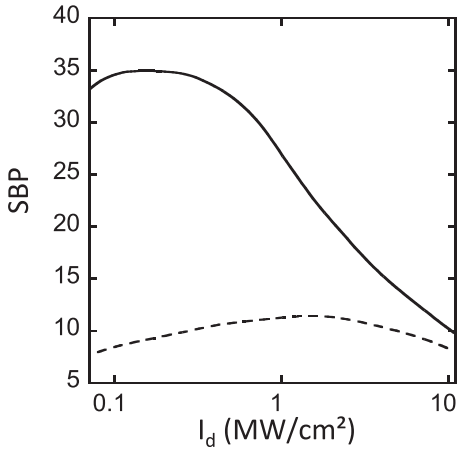

FIG. 5. Slowdown-bandwidth product versus drive intensity for a lattice temperature of 300 K (dashed line) and 150 K (solid line).

150 K and 300 K. For small drive intensities the peak gain and the peak slowdown increase with intensity because the effectiveness of the interference between the dressed states increases, which reduces the peak absorption. For drive intensities of about $I_{\mathrm{d}} = 0.1\ \mathrm{MW/cm^2}$ and above the Autler-Townes splitting increases and thus reduces the peak absorption. In this case, the interference effects between the dressed states become less pronounced and peak slowdown decreases with increasing intensity. The peak gain still increases even when the interference becomes less effective because the Autler-Townes splitting continues to increase with intensity.

The slowdown-bandwidth product (SBP)[51] is an important characteristic for the usefulness of quantum-coherence schemes to slow down pulses as already discussed in Ref. 31. From spectra such as Fig. 3 we obtain the SBP $\omega_{1/2} n_b d \chi_r / d\omega_p$, where $\omega_{1/2}$ is the full width at half maximum (FWHM) of the $h_0^b \leftrightarrow e_1$ resonance and χ_r is the real part of $\mathcal{P}/\mathcal{E}_p$. We investigate here the dependence of the SBP on the drive intensity and the influence of the temperature as shown in Fig. 5 for 300 K and 150 K. Because the measurement of the bandwidth for slowdown is only useful, if the Autler-Townes splitting of the resonance is clearly visible, the product is not calculated for low drive intensities. The increase of the Autler-Townes splitting with increasing drive intensities leads to an increase of the SBP in a drive intensity range in which the slowdown S' already decreases. For still higher intensities the pronounced drop in S' wins over the increasing broadening. Further, the smaller broadening of spectral features for lower temperatures influences the result by increasing the slowdown bandwidth. If the SBP is compared to the one calculated in Ref. 31 for a Λ scheme, we have a tremendous improvement. However, the improvement of the SBP is even more pronounced for lower temperatures. Encouraged by this promising result we investigated the propagation of the probe pulse and calculated the slowdown factor for various propagation conditions as presented in the following section.

B. Slowdown factor due to pulse propagation

The analysis of the performance of the QD molecule for slowing down light is extended by including the effects

of propagation, because in experiments and applications the important information is in the spatiotemporal dynamics of the probe pulse. The drive field is taken as cw or, for numerical reasons, as a pulse much longer than the probe. As shown in Fig. 1 and explained in the following its reasonable to neglect the propagation of the drive field in the growth direction while accounting for propagation of the probe pulse in the plane of the well: The quantum well considered here, which includes the active region, has a width of 30 nm in the growth direction. Even if we assume a structure composed of several quantum wells to achieve an increased confinement factor for the probe pulse, the total width of the active region stays far below 1 μm. Therefore, propagation effects for the drive pulse can be neglected and we concentrate on the propagation of the probe pulse. We assume a quantum well with an extension of 250 μm in the y direction, in which the active region is contained. Further, we assume a long drive pulse of duration 200 ps and a spot radius larger than 250 μm centered on the quantum well. A probe pulse is initialized to occur in the middle of the drive pulse; this defines the propagation distance zero. The finite drive-pulse duration is only introduced for numerical reasons. In an experiment it could be a cw drive.

We compare the propagation results for a $\cosh^{-2}$ probe pulse with a FWHM of 17.6 and 35.3 ps with the results for a cw probe field without propagation effects as described and calculated in the previous section. The calculation of the gain and the slowdown factor due to pulse propagation of the probe pulses is discussed below. The FWHM is given for the field amplitude and corresponds to a FWHM of 12.1 and 24.2 ps for the field intensity, respectively. The calculation is done for a lattice temperature of 300 K. We start the probe pulse at 0 μm with the relative time $t_0' = t_0$ (see time transformation for slowly varying Maxwell equations) and propagate the probe pulse in the relative time t'. After a propagation length d_P we determine the distance in the relative time $\Delta t'$ between the initial and the propagated probe-pulse peak maximum and calculate the slowdown factor $S - n_b$ averaged over the propagation distance. The difference between the initial and the propagated peak maximum of the probe pulse can be used to calculate the amplitude gain of the probe pulse averaged over the propagation distance.

Figure 6 shows the gain and slowdown factor calculated for different drive-pulse intensities and for a propagation distance of $d_P = 1$ μm. Figure 7 shows the same data for a lattice temperature of 150 K; it will be discussed further in connection with the 150 K results below. For the short probe pulse compared to the long probe pulse and the cw probe field, the drive-pulse intensity has to be higher to reach a comparable transparency, so that the dependence of the slowdown factor on the intensity is shifted and damped. The reason for this behavior is that the polarization of the probe pulse needs some time to build up the coherences that lead to the steady-state Autler-Townes splitting and, in turn, to EIT with slowdown. Additionally, the gain and slowdown increase for longer propagation distances. This can be explained with the increasing temporal broadening of the probe pulse for longer propagation distances due to small absorption effects: For the probe pulse with an initial FWHM of 17.6 ps propagation effects lead to a slight temporal broadening and a slightly smaller (temporal) gradient of the

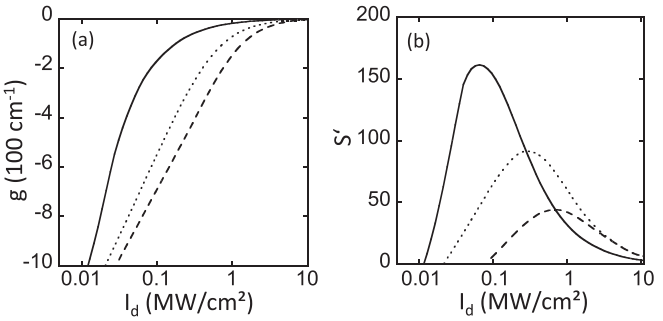

FIG. 6. Gain (a) and slowdown (b) versus drive-pulse intensity after a propagation distance of 1 μm for a $\cosh^{-2}$ probe pulse with a FWHM of 17.6 ps (dashed line) and 35.3 ps (dotted line) and a lattice temperature of 300 K. For comparison, the gain and slowdown factor for a cw probe (black solid line) without propagation effects is plotted.

pulse, resulting in higher gain and slowdown for the spatial propagation. For a probe pulse with an initial FWHM of 35.3 ps these effects are less pronounced due to the longer pulse with a smaller (temporal) gradient of the field.

In Figs. 8–11, we compare the shape of the probe pulse after different propagation distances for different drive-pulse intensities and lattice temperatures. The temporal shape of the probe pulse is shown in *real time* for propagation distances of a few 100 μm. For comparison a reference pulse, i.e., a propagated pulse shape without slowdown, is also plotted. This reference pulse is obtained by propagating the probe field in the host material with refractive index n_b, but without the QD molecules. A temporal shift of the probe-pulse peak against the reference pulse peak to positive times after a spatial propagation corresponds to a slowdown of the probe pulse and a temporal shift to negative times corresponds to a speedup of the probe pulse. Figure 8 contains results for a drive-pulse intensity of 0.7 MW/cm^2 and a maximum propagation distance of 100 μm. The slowdown of the probe pulse is clearly visible and the probe-pulse peak after a propagation distance of 100 μm already has a noticeable separation to the initial probe-pulse peak with a moderate loss of amplitude and only a small distortion. Figure 9 changes the drive-pulse intensity to 1.8 MW/cm^2. In this case, a pulse separation is reached for longer propagation distance, i.e., less efficient slowdown, but with a lower loss of amplitude and a smaller distortion. Therefore, the shape of the probe pulse is plotted for propagation distances up to 250 μm.

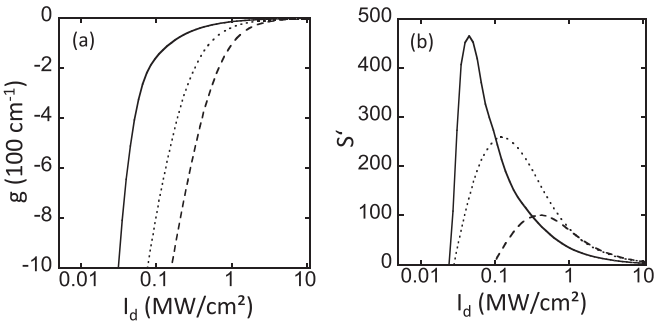

FIG. 7. Same plot as in Fig. 6 for a lattice temperature of 150 K.

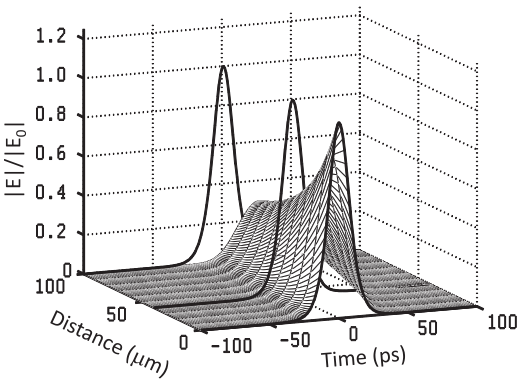

FIG. 8. Temporal shape of the probe-pulse field versus propagation distance for a drive-pulse intensity of 0.7 MW cm^{-2}. The shape of the reference pulse versus propagation distance is plotted at $z = 0$ μm, $z = 50$ μm, and $z = 100$ μm for comparison. The initial shape of the probe and reference pulse is a cosh^{-2}. The lattice temperature is 300 K.

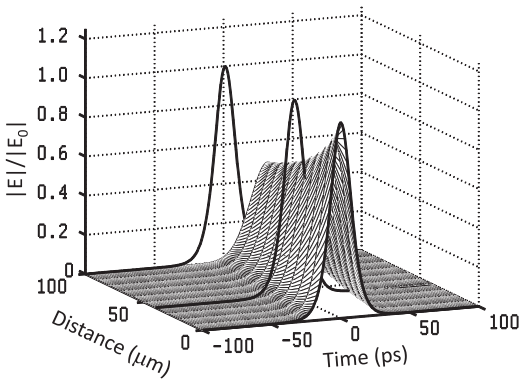

FIG. 10. Temporal shape of the probe-pulse field versus propagation distance for a drive-pulse intensity of 0.7 MW cm^{-2}. The shape of the reference pulse versus propagation distance is plotted at $z = 0$ μm, $z = 50$ μm, and $z = 100$ μm for comparison. The initial shape of the probe and reference pulse is a cosh^{-2}. The lattice temperature is 150 K.

The lower loss of amplitude and the lower distortion is due to the lower absorption at higher intensities already visible in Fig. 6. Therefore, the absorption, i.e., distortion, and the slowdown factor of the probe pulse have to be balanced to obtain decent results for a slow-light application. Here, for both drive-pulse intensities a separation between the initial peak and the propagated peak of the probe pulse is possible with a moderate loss of amplitude.

We also calculated the propagation for a cosh^{-2} probe pulse with a FWHM of 17.6 ps and a cosh^{-2} probe pulse with a FWHM of 35.3 ps for a lattice temperature of 150 K. The gain and slowdown factor are calculated for a set of drive-pulse intensities and for a propagation distance of $d_P = 1$ μm and shown in Fig. 7. Furthermore the cw probe result is plotted for comparison. We obtain for gain and slowdown factor plots generally the same qualitative behavior as described for the case of 300 K (see Fig. 6), but better results, i.e., less absorption and more pronounced slowdown. This improvement is also evident from the comparison of the probe-pulse shape between different propagation distances in Figs. 10 and 11: For a drive-pulse intensity of 0.7 MW/cm^2 and 1.8 MW/cm^2, the shape of the probe pulses is plotted after propagation distances up to 100 and 250 μm, respectively. Again we obtain the same qualitative behavior between the two drive-pulse intensities as already analyzed for the case of 300 K. In addition, for a lattice temperature of 150 K less absorption and higher slowdown are obtained and thus a pulse separation with a smaller loss of amplitude and a smaller pulse distortion can be realized. In Fig. 12 the results of Fig. 11 are shown as a two-dimensional graph, for better quantitative comparison. Now, the shape of the probe pulse is shown vs relative time after a propagation distance of 0, 100, 200, and 250 μm. Because the shape of the probe pulse is plotted against the relative time, a temporal shift of the probe-pulse peak to positive relative times after a spatial propagation corresponds to a slowdown of the probe pulse and a temporal shift to negative relative times corresponds to a speedup of the probe pulse. Figure 12 shows that the separation of the pulse peaks is about 29 ps after 250 μm with a small loss of amplitude and negligible distortion. These numerical values are promising for slow-light applications.

To conclude this section, we would like to give some numbers regarding effective dephasing rates for our QD molecule system and setup. We determined polarization dephasing rates for three transitions: the quantum coherence $e_0 \leftrightarrow e_1$, the

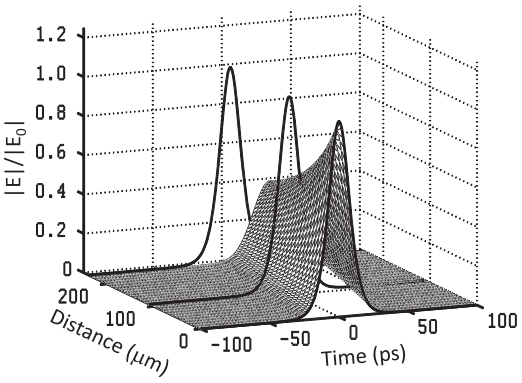

FIG. 9. Same as Fig. 8 for a drive-pulse intensity of 1.8 MW cm^{-2}. The reference pulse is shown for $z = 0$ μm, $z = 100$ μm, and $z = 200$ μm.

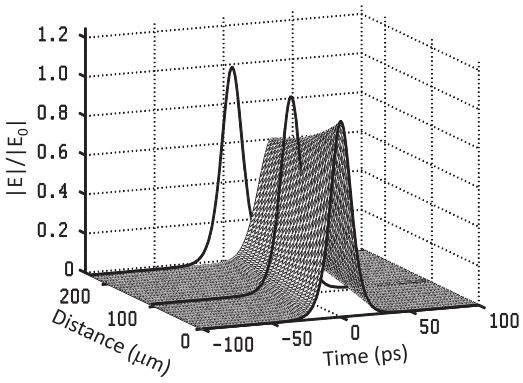

FIG. 11. Same as Fig. 10 for a drive-pulse intensity of 1.8 MW cm^{-2}. The reference pulse is shown for $z = 0$ μm, $z = 100$ μm, and $z = 200$ μm.

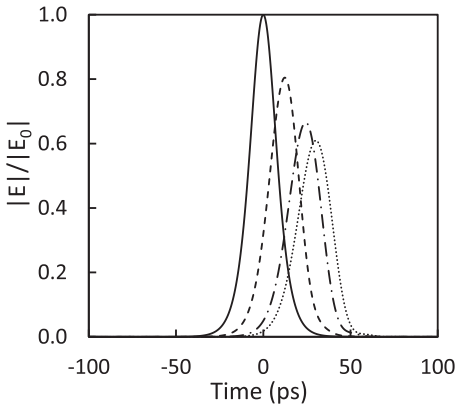

FIG. 12. Temporal field shape of the probe pulse for a drive-pulse intensity of 1.8 MW/cm^2 after propagation distance of 0 μm (solid), 100 μm (dashed), 200 μm (dashed-dotted), 250 μm (dotted). The initial shape of the probe pulse is a cosh^{-2}. The lattice temperature is 150 K.

probe transition $h_0 \leftrightarrow e_1$, and the drive transition $h_0 \leftrightarrow e_0$. As in the calculations for Figs. 8–11, we used an extremely long drive pulse, but also a long probe pulse to mimic cw excitation conditions. The pulse frequencies ω_d and ω_p were chosen to be resonant to the renormalized transition energies corresponding to these excitation conditions. We then fit polarization decay rates γ_{e_0,e_1}, γ_{h_0,e_1}, γ_{h_0,e_0} to the polarization dephasing contributions S_{e_0,e_1}, S_{h_0,e_1}, and S_{h_0,e_0}, respectively. Typical values of the dephasing for the quantum coherence are around $\gamma_{e_0,e_1} \equiv \gamma_{\rm nr} \approx 0.01$ ps^{-1} and the dephasing on the drive and probe transitions is generally on the order of $\gamma \approx 0.5$ ps^{-1} for the range of drive intensities and temperatures (150 K and 300 K) considered here. The dephasing rates of the drive and probe transitions are typical of QDs, whereas the comparatively small dephasing rate of the quantum coherence is due to the design of the QD molecule and the chosen setup. The dephasing of the quantum coherence in the QD molecule obtained from our microscopic calculation at and above 150 K is still quite a bit slower than the dephasing rate 0.125 ns^{-1} assumed in a recent AMO-like calculation of EIT-based slow light in single QDs.[28] Such a slow dephasing along with lifetime-limited linewidths, which were also assumed in Ref. 28, are generally realized only at very low temperatures.

V. COMPARISON TO A SINGLE QD

Here we wish to compare the results for pulse slowdown in the optimized QD molecule with earlier results on QDs. First, in the Λ schemes for an ensemble of single QDs, as investigated in our earlier Refs. 25,31, and 32, the quantum coherence connects two hole states and is therefore susceptible to the same dephasing contributions as the drive or probe (electron-hole) polarization, where the dominant contribution of the dephasing comes from the hole states because they are closely spaced, and because of the polaronic broadening the electron-phonon interaction can efficiently couple them. In this case, a short drive pulse is necessary to slow down the probe pulse,[31,32] but the time window during which the probe pulse is slowed down is too short.[33] To highlight the slowdown achievable in QD molecules with cw drive fields we would like to compare them with single QDs for the same quantum-coherence scheme, namely a V scheme. Our choice of V scheme is also supported by investigations of quantum-coherence schemes in single QDs which found that the structural QD parameters can generally be more easily optimized for V schemes than for other schemes.[27,30] In the following we investigate the pulse slowdown for V schemes using single QDs in the same manner as for the QD molecules. For the purpose of this section, it is not necessary to design novel QD molecule structures using finite model potentials and wave functions that are checked against $k \cdot p$ calculations. Instead, for simplicity, we work with a simpler QD model with a harmonic oscillator confinement potential. This model was used, e.g., in Ref. 25.

A. Single QD model for a V scheme

The QD model and the calculation of the pulse slowdown for V schemes is similar between single QDs and QD molecules. Here, we highlight only the differences. We assume cylindrical single QDs described by the Hamiltonian (A1) in envelope approximation, but without the finite potential (A2). Instead, we replace the in-plane confinement potential in Eq. (A14) with a harmonic oscillator confinement potential. This is a good approximation, because measurements of the dependence of the lowest bound states in a QD are also in agreement with a spectrum of a harmonical oscillator.[25] The in-plane Hamiltonian can be solved by separating the radial and angular dependence using Hermite polynomials as also described in Ref. 25. This approximation would be inappropriate for QD molecules, because the determination of wave functions and energy levels from a *finite* confinement potential for each single QD is necessary to calculate the wave functions and energy levels of the electronically coupled QDs (i.e., QD molecules).

We assume an ensemble of InGaAs-based QDs embedded in a GaAs quantum well with a width of 16 nm, which leads to three confined electron and hole states. Thus, we have one doubly degenerate excited state and one ground state with the energy values in Table II. The lineup of the levels is shown schematically in Fig. 13. Using an analytical model of cylindrical QDs only diagonal transitions are dipole allowed because of symmetry considerations. However, to realize a V scheme one needs off-diagonal interband transitions. We achieve this by including a symmetry-breaking static electric field. To make off-diagonal dipole matrix elements appreciable, we use an external electric field in the plane of the quantum well with a field strength of 4.0 mV nm^{-1}. The calculated dipole matrix elements make a V scheme with a drive pulse between the electron and hole ground state and a probe pulse between the hole ground state and the excited electron states possible. The quantum coherence of the V

TABLE II. Electron (e) and hole (h) energies of single-particle states in the single QD.

State	E_e (meV)	State	E_h(meV)
e_0	−150	h_0	50
$e_{1/2}$	−60	$h_{1/2}$	20

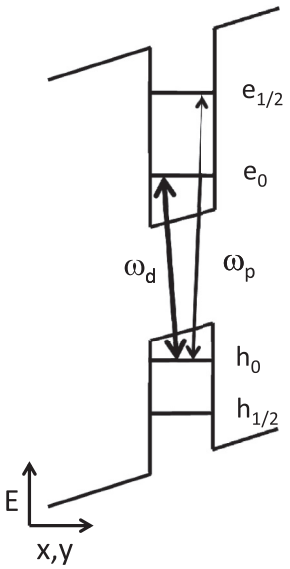

FIG. 13. Schematic picture of the geometry of the single QD described in the text. The resonant probe and drive fields in a V-type quantum-coherence scheme are also shown.

scheme is between the electron ground and the excited electron states. The energy gap between the electron and hole ground state is taken to be 1.2 eV.

As shown in Table II, we assume a *deep* confinement of the QD states. This choice is necessary to obtain noticeable slowdown in our single QD V-scheme setup: As already explained in Sec. III B the dominant dephasing processes of our single QD V scheme setup are those carrier-phonon dephasing processes which are associated with real carrier-phonon scattering transitions. For a shallow confinement of the QD states the hole-intersubband and the electron-intersubband contributions would be of equal size due to the small energy spacing of the hole and the electron states.[33] For a deep confinement of the QD states the energy spacing of the electron states is high enough to suppress the electron-intersubband contribution. Thus, the carrier-phonon dephasing of the quantum coherence is small compared to the carrier-phonon dephasing of the probe polarization for a deep QD, but for a shallow QD the two carrier-phonon dephasing rates would be of equal size.

B. Numerical results for the single QD V scheme

For the single QD we first investigate peak gain and peak slowdown as done in Fig. 4 by comparing a lattice temperature of 150 K with a lattice temperature of 300 K. For the calculation of the gain and the slowdown factor, we use the semiconductor Bloch equations (5)–(8) including a microscopic scattering and dephasing contribution as described in Sec. III B. The peak gain and peak slowdown vs drive intensity are shown in Fig. 14. Below a drive intensity of 0.1 MW/cm^2 we find a significant peak absorption without peak slowdown for both lattice temperatures. Above a drive intensity of 0.1 MW/cm^2 the peak slowdown factor for similar peak absorption values is higher for lower temperatures. This result again is obtained because the average phonon occupation is reduced for lower temperatures, and a smaller carrier-phonon dephasing rate

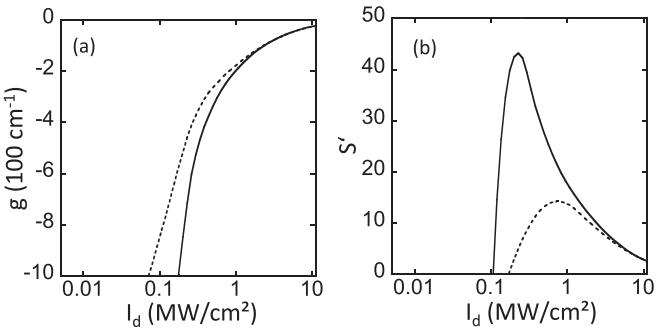

FIG. 14. Peak gain (a) and peak slowdown (b) versus drive intensity for a lattice temperature of 150 K (solid line) and 300 K (dashed line) for a deep single QD.

results for all polarizations. This reduction is proportionally less pronounced for the *interband* and proportionally more pronounced for the *quantum coherence*. The dephasing processes of the quantum coherence which are associated with real carrier-phonon scattering transitions are significantly reduced. These processes no longer dominate over carrier-carrier and pure-dephasing carrier-phonon processes of the quantum coherence. However, an effectively long dephasing time for (realistic) slow-light applications is still not reached.

C. Comparison between a V scheme in a single QD and a QD molecule

Finally, we compare the results of the QD molecule and the deep single QD for a lattice temperature of 150 K. In Fig. 15 the peak gain and peak slowdown versus drive intensity is plotted for both setups. A tremendous improvement of the peak slowdown factor for similar peak absorptions values for the QD molecule compared to the deep single QD is visible. This improvement can be explained in the following way: The negligible wave-function overlap between the states of the $e_0 \leftrightarrow e_1$ transition of the V system in the QD molecule has a huge influence on the electron-phonon *and electron-electron* dephasing contributions of the quantum coherence. This influence reduces the dephasing rate of the quantum coherence much more than the dephasing rate of the interband probe polarization. Therefore, the comparison between the results of single QDs and QD molecules shows

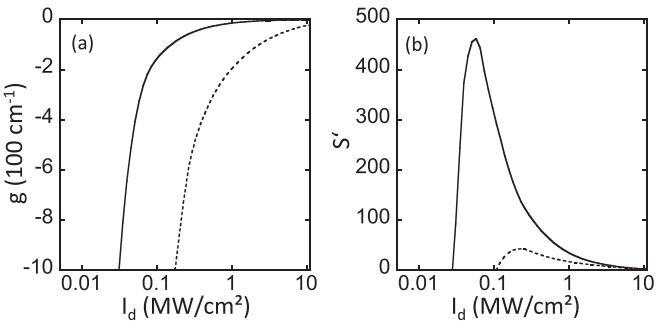

FIG. 15. Peak gain (a) and peak slowdown (b) versus drive intensity for the QD molecule (solid line) and the deep single QD. The lattice temperature is 150 K.

that an effectively long dephasing time can be engineered only by using suitable QD *molecules*.

VI. CONCLUSION

In this paper we presented a microscopic analysis of quantum-coherence schemes, in particular EIT and group-velocity slowdown, in a special double-QD molecule design. We incorporated scattering and dephasing effects, including polaronic effects in QDs, into the equations of motion for the relevant polarizations and distribution functions. We used a quasianalytic model for QD single-particle states with parameters adjusted to the results of $k \cdot p$ calculations for a realistic InGaAs-based QD. The design of the double-QD molecule was geared towards achieving a long-lived quantum coherence in a V scheme involving two electronic levels localized at the individual QDs and a delocalized hole level. Starting from the quasianalytic QD model we constructed the states of the QD molecule and used these as input in the equations of motion for polarizations and distribution functions. Choosing probe and drive fields suitable for a V scheme consisting of the delocalized hole level and the two localized electron levels, we found cw slowdown factors and SBPs of the QD molecule that are far better than our previous results on Λ schemes or results achieved by V schemes in single QDs as presented in Sec. V. We further combined the microscopic material equations with a numerical calculation of the propagating probe pulse and showed that a clear separation of the slowed-down pulse with a reference pulse can be achieved over distances of a few μm with acceptable pulse distortion and absorption. We emphasized that this result was made possible by the design of the QD molecule that yields a comparatively long dephasing time on the quantum coherence. Importantly, the dephasing contributions that largely determine the figures of merit for the slowdown were not taken as constant rates, but arose from the microscopic treatment of the underlying interaction processes for a sufficiently realistic QD model.

ACKNOWLEDGMENTS

This work was supported in part by Sandia's Solid-State Lighting Science Center, an Energy Frontier Research Center (EFRC) funded by the U.S. Department of Energy, Office of Science, Office of Basic Energy Sciences.

APPENDIX A: ELECTRONIC STRUCTURE OF QD MOLECULES

This appendix gives details of our calculation of the wave functions and energies of QD molecules. Since we are interested in the qualitative properties of QD molecules, and wish to be able to easily describe the structural parameters (i.e., different QD sizes and distances between the two QDs), we use a simple and semianalytical approximation for the description of the QDs contained in the QD molecules. We stress that no band-mixing due to strain or piezoelectric effects are included, but the parameters used in the model have been chosen to compare well to a QD calculated by $k \cdot p$ theory.

1. Electronic structure of a cylindrical QD

We assume a cylindrical QD with a confinement potential of depth. For the Hamiltonian of the cylindrical QD in envelope approximation we use

$$H = -\frac{\hbar^2}{2m}\nabla^2 + V(r,z), \tag{A1}$$

where the Laplacian ∇^2 and

$$V(r,z) = \begin{cases} 0 & \text{for} \quad |z| > a \quad \text{or} \quad |r| > b, \\ -V_0 & \text{for} \quad |z| < a \quad \text{and} \quad |r| < b, \end{cases} \tag{A2}$$

are expressed in cylindrical coordinates. The heights of the QD in z direction is $h = 2a$, the diameter is $2b$, and V_0 is the depth of the confinement potential. The wave function Φ_{3D} of the Schrödinger equation

$$H\Phi_{3D} = E\Phi_{3D} \tag{A3}$$

has to be understood as an envelope function and m as an effective mass.

We assume that the height is much smaller than the diameter of the QD. Therefore, the electrons and holes are strongly localized in the growth direction z. If we assume the separability of the wave function for the in-plane and the z direction, the three-dimensional Schrödinger equation reduces to a two- and a one-dimensional problem. Thus, we can write for the wave function

$$\Phi_{3D}(r,\varphi,z) = N\,\Phi_{\parallel}(r,\varphi)\Phi_{\perp}(z), \tag{A4}$$

where N is a normalization constant. Furthermore, we used in the z direction $\int \Phi^*_{\perp}(z)V(r,z)\Phi_{\perp}(z)dz \approx -V_0\Theta(b-|r|)$ and the corresponding approximation for the in-plane direction to obtain a self-consistent set of equations.

For the Schrödinger equation in the z direction we have

$$\left[-\frac{\hbar^2}{2m}\frac{\partial^2}{\partial z^2} + \tilde{V}_{\perp}\,\Theta(a-|z|)\right]\Phi_{\perp}(z) = E_{\perp}\Phi_{\perp}(z). \tag{A5}$$

Here, $\tilde{V}_{\perp} = -V_0 + T_{\parallel}$ is an effective one-dimensional potential that contains the in-plane kinetic energy $T_{\parallel} = \tilde{V}_{\parallel} - E_{\parallel}$ which, in turn, depends on the in-plane eigenenergy $E_{\parallel}$. Since these kinetic energies $T_{\parallel}$ are not known, we use an iteration procedure to calculate the in-plane and z eigenenergies. We start the iteration by setting $\tilde{V}_{\perp}$ equal to $-V_0$. For the solution we obtain for the symmetric eigenstates,

$$\begin{aligned}\Phi^S_{\perp,n}(z) = {} & B\Theta(|z|-a)\cos(k_n a)e^{\kappa_n(a-|z|)} \\ & + B\Theta(a-|z|)\cos(k_n z),\end{aligned} \tag{A6}$$

and for the antisymmetric eigenstates,

$$\begin{aligned}\Phi^A_{\perp,n}(z) = {} & C\Theta(|z|-a)\mathrm{sgn}(z)\sin(k_n a)e^{\kappa_n(a-|z|)} \\ & + C\Theta(a-|z|)\sin(k_n z).\end{aligned} \tag{A7}$$

Here B and C are normalization constants and we have defined

$$\kappa_n = \frac{\sqrt{2m|E_{\perp,n}|}}{\hbar}, \tag{A8}$$

$$k_n = \frac{\sqrt{2m(|\tilde{V}_{\perp}| - |E_{\perp,n}|)}}{\hbar}. \tag{A9}$$

The eigenvalues $E_{\perp,n}$ can be determined by the intersection $s_n = k_n a$ of the curves

$$f(ka) = \tan(ka), \tag{A10}$$

$$g^S(ka) = \frac{\sqrt{(k_0 a)^2 - (ka)^2}}{(ka)}, \tag{A11}$$

or

$$g^A(ka) = \frac{-(ka)}{\sqrt{(k_0 a)^2 - (ka)^2}}, \tag{A12}$$

where $k_0 = \sqrt{2m|\tilde{V}_\perp|/\hbar}$. We obtain the eigenvalues

$$E_{\perp,n} = \frac{\hbar^2 s_n^2}{2ma^2} - |\tilde{V}_\perp|. \tag{A13}$$

For the Schrödinger equation in the in-plane direction we have

$$\left\{-\frac{\hbar^2}{2m}\left[\frac{1}{r}\frac{\partial}{\partial r}\left(r\frac{\partial}{\partial r}\right) + \frac{1}{r^2}\frac{\partial^2}{\partial\varphi^2}\right] + \tilde{V}_\parallel \Theta(b-r)\right\}\Phi_\parallel(r,\varphi) = E_\parallel \Phi_\parallel(r,\varphi). \tag{A14}$$

The effective potential $\tilde{V}_\parallel = -V_0 + T_\perp$ again includes a contribution from the kinetic energy in the growth direction, which depends on the solution of the eigenvalue problem in the z direction, $T_\perp = \tilde{V}_\perp - E_\perp$. We start the iteration by setting $\tilde{V}_\parallel$ equal to $-V_0$. Because of the symmetry of the potential around the growth direction, the Hamiltonian commutes with the components of the angular momentum operator ($[H,l_z] = 0$). Therefore, the two-dimensional Schrödinger equation for the angular momentum projection quantum number m_l reduces to an effective one-dimensional Schrödinger equation. Resorting the terms we obtain

$$\left[-\frac{\hbar^2}{2m}\left(\frac{1}{r}\frac{\partial}{\partial r} + \frac{\partial^2}{\partial r^2}\right) + \tilde{V}_\parallel\Theta(b-r) + \frac{\hbar^2}{2m}\frac{m_l^2}{r^2}\right]\tilde{\Phi}_\parallel(r) = E_\parallel\tilde{\Phi}(r), \tag{A15}$$

where

$$\Phi_\parallel(r,\varphi) = \frac{1}{\sqrt{2\pi}} e^{im\varphi}\tilde{\Phi}_{\parallel,m}(\varphi) \tag{A16}$$

This equation can be cast into the form of a Bessel differential equation. A solution of this differential equation inside the QD is the Bessel function in mth order of the first kind $J_m(kr)$. Therefore, we obtain inside the QD

$$\widetilde{\Phi}_{\parallel,m}(r) = A J_m(kr). \tag{A17}$$

A solution outside the QD is the modified Bessel function $K_m(\kappa_r r)$. Therefore, we obtain outside the QD

$$\widetilde{\Phi}_{\parallel,m}(r) = B K_m(\kappa_r r). \tag{A18}$$

At $r = b$, the wave functions $\Psi'_\parallel$ and $\Psi_\parallel$ have to be continuous. With $k_0^2 = \frac{2m}{\hbar^2}(-\tilde{V}_\parallel)$ and $\kappa_r = \sqrt{k_0^2 - k^2}$, the continuity condition yields

$$N(k) = \frac{J'_m(kR)}{J_m(kR)} - \frac{K'_m\left(\sqrt{k_0^2 - k^2}R\right)}{K_m\left(\sqrt{k_0^2 - k^2}R\right)} = 0. \tag{A19}$$

All k_n between 0 and k_0 with $N(k) = 0$ are allowed. For the eigenvalues of the two-dimensional problem we obtain

$$E_{\parallel,n} = \frac{\hbar^2\left(k_n^2 - k_0^2\right)}{2m}. \tag{A20}$$

In summary, we have energy levels $E_{\parallel,n,m}$ and wave functions $\Phi_{\parallel,n,m}$ with the quantum numbers n and m. The states with different m and the same n are degenerate.

For the approximate solution of the three-dimensional problem we have to solve the one- and two-dimensional eigenvalues in a self-consistent fashion by determining the updated potentials for the next iteration step from the eigenenergies of the previous iteration. The procedure is quite efficient, and one obtains converged eigenvalues $E_{n_z n_r m}$ and wave functions $\Phi_{n_z n_r m}$ for the pillbox-shaped QD after only a few iteration steps. The resulting energies and wave functions, obtained using optimized effective parameters, have been checked against $k \cdot p$ calculations,[45,46] which include strain and piezoelectric effects.

2. Electronic structure of a QD molecule

After introducing the pillbox model for the electronic structure of QDs, we now couple these QDs to molecules. For this purpose we introduce an ansatz similar to the linear combination of atomic orbitals.

For a detailed description of the calculation we assume a QD molecule consisting of two QDs, labeled 1 and 2. For QD 1 and 2 we assume N and M bound states, respectively. Further, for the uncoupled QDs, we label the wave functions Φ_1^n and Φ_2^m, the eigenvalues ε_1^n and ε_2^m, and the potential V_a and V_b, respectively. To determine the envelope wave functions Φ, and the corresponding eigenvalues E, of the electronically coupled QDs we use a superposition of the following form:

$$\Phi = \sum_n c_1^n \Phi_1^n + \sum_m c_2^m \Phi_2^m. \tag{A21}$$

With the Hamiltonian

$$(H_0 + V_a + V_b)\Phi = E\Phi, \tag{A22}$$

we can apply a multiplication of $(\Phi_1^j)^*$ and a multiplication of $(\Phi_2^k)^*$, respectively. Therefore, we obtain in matrix notation

$$\begin{pmatrix} M_1^{jn} & M_2^{jm} \\ M_3^{kn} & M_4^{km} \end{pmatrix}\begin{pmatrix} c_1^n \\ c_2^m \end{pmatrix} = \begin{pmatrix} A_1^{jn} & A_2^{jm} \\ A_3^{kn} & A_4^{km} \end{pmatrix} E \begin{pmatrix} c_1^n \\ c_2^m \end{pmatrix}, \tag{A23}$$

where

$$M_1^{jn} = \varepsilon_1^n \delta_{jn} + \left\langle \Phi_1^j \middle| V_b \middle| \Phi_1^n \right\rangle, \tag{A24}$$

$$M_2^{jm} = \varepsilon_2^m \left\langle \Phi_1^j \middle| \Phi_2^m \right\rangle + \left\langle \Phi_1^j \middle| V_a \middle| \Phi_2^m \right\rangle, \tag{A25}$$

$$M_3^{kn} = \varepsilon_1^n \left\langle \Phi_2^k \middle| \Phi_1^n \right\rangle + \left\langle \Phi_2^k \middle| V_b \middle| \Phi_1^n \right\rangle, \tag{A26}$$

$$M_4^{km} = \varepsilon_2^m \delta_{km} + \left\langle \Phi_2^k \middle| V_a \middle| \Phi_2^m \right\rangle, \tag{A27}$$

and $A_1^{jn} = \delta_{jn}$, $A_2^{jm} = \langle \Phi_1^j | \Phi_2^m \rangle$, $A_3^{kn} = \langle \Phi_2^k | \Phi_1^n \rangle$, as well as $A_4^{km} = \delta_{km}$. This generalized eigenvalue problem can be solved numerically with an eigenvalue solver.[52] Because in this case matrix A is invertible, its possible to reduce the generalized eigenvalue problem to an (ordinary) eigenvalue

problem. Therefore, we have to solve

$$\left[\begin{pmatrix} A_1^{jn} & A_2^{jm} \\ A_3^{kn} & A_4^{km} \end{pmatrix}^{-1} \begin{pmatrix} M_1^{jn} & M_2^{jm} \\ M_3^{kn} & M_4^{km} \end{pmatrix}\right] \begin{pmatrix} c_1^n \\ c_2^m \end{pmatrix} = E \begin{pmatrix} c_1^n \\ c_2^m \end{pmatrix}. \tag{A28}$$

The eigenvalues and eigenfunctions of this equation have to be understood as the single-particle result for the electronic structure of the QD molecule, which can then be used as input in the many-particle semiconductor Bloch equations.

Furthermore, we want to consider a sufficiently weak external electric field, i.e., an electric field that can be included in the LCAO calculation of the QD molecules. For electrons, one includes in the potential $V_a + V_b$ in (A22) a contribution from the electric field Fz, where F is the electric field. For holes, the sign of the electric potential is reversed. The results of this semianalytical approach for QD molecules without electric field were again checked against the $k \cdot p$ calculation.[45,46] The approach was found to yield a qualitatively correct description of the electronic structure of the QD molecules studied in this paper.

APPENDIX B: CORRELATION CONTRIBUTIONS DUE TO CARRIER-PHONON AND CARRIER-CARRIER INTERACTIONS

We investigate a QD/QD molecule of the ensemble with M^e electron and M^h hole states embedded in a quantum well. We make a single-band approximation for the quantum well and assume that all electron and hole states are spin or pseudospin degenerate, respectively. So every state in the QD/QD molecule can be labeled by $\lambda = (b,\vec{k} = m,s)$, where $b \in \{c,v\}$ is the band index, $m \in \{1,\ldots,M^e\}/\{1,\ldots,M^h\}$, $s \in \{\uparrow,\downarrow\}$. States in the quantum well are labeled by $\lambda = (b,\vec{k} = \vec{k}_\parallel,s)$. Thus, we introduce the notation λ_1 with $\lambda_1 = (b_1,\vec{k}_1,s)$ for all states. With this unified index $\lambda_1 = (b_1,\vec{k}_1,s_1)$ a simplification of the carrier-phonon interaction matrix elements

$$M^{\lambda_1\lambda_2}_{\lambda_3\lambda_4} = M^{\lambda_1\lambda_2}_{\lambda_3\lambda_4}\delta_{b_1b_2}\delta_{b_3b_4} \tag{B1}$$

and the carrier-carrier interaction matrix elements

$$W^{\lambda_1\lambda_2}_{\lambda_3\lambda_4} = W^{\lambda_1\lambda_2}_{\lambda_3\lambda_4}\delta_{b_1b_2}\delta_{b_3b_4} \tag{B2}$$

follows. With the derivation described in Sec. III B and a generalized notation $\rho_{\lambda_1\lambda_2}$ for the density matrix we obtain for dephasing and scattering processes due to the carrier-phonon interaction in Markov approximation the following set of equations:

$$S^{cp}_{\lambda_1\lambda_2} = \frac{\pi}{\hbar}\sum_{\lambda_3}\rho_{\lambda_3\lambda_2}(t)K_1^{cp} + \frac{\pi}{\hbar}\sum_{\lambda_3}\rho_{\lambda_1\lambda_3}(t)K_2^{cp} - \frac{\pi}{\hbar}\sum_{\lambda_3}\rho^*_{\lambda_3\lambda_2}(t)K_3^{cp} - \frac{\pi}{\hbar}\sum_{\lambda_3}\rho^*_{\lambda_1\lambda_3}(t)K_4^{cp}, \tag{B3}$$

where

$$K_1^{cp} = \sum_{\lambda_4\lambda_5} M^{\lambda_1\lambda_5}_{\lambda_4\lambda_3}\rho^*_{\lambda_4\lambda_5}(t)\sum_{\pm}\left(N + \frac{1}{2} \mp \frac{1}{2}\right) g\left(-\widetilde{\varepsilon}_{\lambda_5} + \widetilde{\varepsilon}^*_{\lambda_3} \pm \hbar\omega_{LO}\right), \tag{B4}$$

$$K_2^{cp} = \sum_{\lambda_4\lambda_5} M^{\lambda_3\lambda_5}_{\lambda_4\lambda_2}\rho^*_{\lambda_4\lambda_5}(t)\sum_{\pm}\left(N + \frac{1}{2} \mp \frac{1}{2}\right) g\left(-\widetilde{\varepsilon}_{\lambda_3} + \widetilde{\varepsilon}^*_{\lambda_4} \mp \hbar\omega_{LO}\right), \tag{B5}$$

$$K_3^{cp} = \sum_{\lambda_4\lambda_5} M^{\lambda_1\lambda_5}_{\lambda_4\lambda_3}\rho_{\lambda_4\lambda_5}(t)\sum_{\pm}\left(N + \frac{1}{2} \mp \frac{1}{2}\right) g\left(-\widetilde{\varepsilon}_{\lambda_5} + \widetilde{\varepsilon}^*_{\lambda_3} \mp \hbar\omega_{LO}\right), \tag{B6}$$

$$K_4^{cp} = \sum_{\lambda_4\lambda_5} M^{\lambda_3\lambda_5}_{\lambda_4\lambda_2}\rho_{\lambda_4\lambda_5}(t)\sum_{\pm}\left(N + \frac{1}{2} \mp \frac{1}{2}\right) g\left(-\widetilde{\varepsilon}_{\lambda_3} + \widetilde{\varepsilon}^*_{\lambda_4} \pm \hbar\omega_{LO}\right). \tag{B7}$$

Here, we have used the abbreviation $g(z) = \frac{i}{\pi z}$, and, as discussed in connection with Eq. (9), $\widetilde{\varepsilon}_{\lambda_1} = \varepsilon_{\lambda_1} + \Delta\varepsilon - i\Gamma$ is a complex single-particle energy with an energy shift $\Delta\varepsilon$ and a damping Γ, which represents an energetic broadening and thus a finite quasiparticle lifetime due to the electron-phonon interaction.

Further, we need an expression for dephasing and scattering processes due to carrier-carrier interaction as described in Sec. III B. For the carrier-carrier interaction in Markov approximation one obtains

$$S^{cc}_{\lambda_1\lambda_2} = \frac{\pi}{\hbar}\sum_{\lambda_3\ldots\lambda_9}\left(\rho_{\lambda_3\lambda_2}(t)K_1^{cc} + \rho_{\lambda_1\lambda_3}(t)K_2^{cc} - \rho^*_{\lambda_3\lambda_2}(t)K_3^{cc} - \rho^*_{\lambda_1\lambda_3}(t)K_4^{cc}\right), \tag{B8}$$

where

$$K_1^{cc} = W^{\lambda_6\lambda_7}_{\lambda_1\lambda_4}\left(W^{\lambda_9\lambda_8}_{\lambda_3\lambda_5}\right)^*\rho^*_{\lambda_4\lambda_5}(t)\rho_{\lambda_9\lambda_6}(t)\rho^*_{\lambda_7\lambda_8}(t)g\left(-\widetilde{\varepsilon}_{\lambda_5} + \widetilde{\varepsilon}^*_{\lambda_9} - \widetilde{\varepsilon}_{\lambda_8} + \widetilde{\varepsilon}^*_{\lambda_3}\right) - W^{\lambda_6\lambda_7}_{\lambda_1\lambda_4}\left(W^{\lambda_9\lambda_8}_{\lambda_3\lambda_5}\right)^*\rho^*_{\lambda_4\lambda_8}(t)\rho_{\lambda_9\lambda_6}(t)\rho^*_{\lambda_7\lambda_5}(t)g\left(-\widetilde{\varepsilon}_{\lambda_5} + \widetilde{\varepsilon}^*_{\lambda_9} - \widetilde{\varepsilon}_{\lambda_8} + \widetilde{\varepsilon}^*_{\lambda_3}\right), \tag{B9}$$

$$K_2^{cc} = W^{\lambda_6\lambda_7}_{\lambda_3\lambda_4}\left(W^{\lambda_9\lambda_8}_{\lambda_2\lambda_5}\right)^*\rho^*_{\lambda_4\lambda_5}(t)\rho_{\lambda_9\lambda_6}(t)\rho^*_{\lambda_7\lambda_8}(t)g\left(-\widetilde{\varepsilon}_{\lambda_3} + \widetilde{\varepsilon}^*_{\lambda_4} - \widetilde{\varepsilon}_{\lambda_6} + \widetilde{\varepsilon}^*_{\lambda_7}\right) - W^{\lambda_6\lambda_7}_{\lambda_3\lambda_4}\left(W^{\lambda_9\lambda_8}_{\lambda_2\lambda_5}\right)^*\rho^*_{\lambda_4\lambda_8}(t)\rho_{\lambda_9\lambda_6}(t)\rho^*_{\lambda_7\lambda_5}(t)g\left(-\widetilde{\varepsilon}_{\lambda_3} + \widetilde{\varepsilon}^*_{\lambda_4} - \widetilde{\varepsilon}_{\lambda_6} + \widetilde{\varepsilon}^*_{\lambda_7}\right), \tag{B10}$$

$$K_3^{cc} = W_{\lambda_1\lambda_4}^{\lambda_6\lambda_7}\left(W_{\lambda_3\lambda_5}^{\lambda_9\lambda_8}\right)^* \rho_{\lambda_4\lambda_5}(t)\rho^*_{\lambda_9\lambda_6}(t)\rho_{\lambda_7\lambda_8}(t)g\left(-\widetilde{\varepsilon}_{\lambda_5} + \widetilde{\varepsilon}^*_{\lambda_9} - \widetilde{\varepsilon}_{\lambda_8} + \widetilde{\varepsilon}^*_{\lambda_3}\right) - W_{\lambda_1\lambda_4}^{\lambda_6\lambda_7}\left(W_{\lambda_3\lambda_5}^{\lambda_9\lambda_8}\right)^* \rho_{\lambda_4\lambda_8}(t)\rho^*_{\lambda_9\lambda_6}(t)\rho_{\lambda_7\lambda_5}(t)g\left(-\widetilde{\varepsilon}_{\lambda_5} + \widetilde{\varepsilon}^*_{\lambda_9} - \widetilde{\varepsilon}_{\lambda_8} + \widetilde{\varepsilon}^*_{\lambda_3}\right), \tag{B11}$$

$$K_4^{cc} = W_{\lambda_3\lambda_4}^{\lambda_6\lambda_7}\left(W_{\lambda_2\lambda_5}^{\lambda_9\lambda_8}\right)^* \rho_{\lambda_4\lambda_5}(t)\rho^*_{\lambda_9\lambda_6}(t)\rho_{\lambda_7\lambda_8}(t)g\left(-\widetilde{\varepsilon}_{\lambda_3} + \widetilde{\varepsilon}^*_{\lambda_4} - \widetilde{\varepsilon}_{\lambda_6} + \widetilde{\varepsilon}^*_{\lambda_7}\right) - W_{\lambda_3\lambda_4}^{\lambda_6\lambda_7}\left(W_{\lambda_2\lambda_5}^{\lambda_9\lambda_8}\right)^* \rho_{\lambda_4\lambda_8}(t)\rho^*_{\lambda_9\lambda_6}(t)\rho_{\lambda_7\lambda_5}(t)g\left(-\widetilde{\varepsilon}_{\lambda_3} + \widetilde{\varepsilon}^*_{\lambda_4} - \widetilde{\varepsilon}_{\lambda_6} + \widetilde{\varepsilon}^*_{\lambda_7}\right). \tag{B12}$$

*hcsch@physik.uni-kl.de

[1] M. Fleischhauer, A. Imamoglu, and J. P. Marangos, Rev. Mod. Phys. **77**, 633 (2005).
[2] S. E. Harris, J. E. Field, and A. Imamoglu, Phys. Rev. Lett. **64**, 1107 (1990).
[3] M. O. Scully, S. Y. Zhu, and A. Gavrielides, Phys. Rev. Lett. **62**, 2813 (1989).
[4] J. P. Marangos, J. Mod. Opt. **45**, 471 (1998).
[5] J. Mompart and R. Corbalan, J. Opt. B: Quantum Semiclassical Opt. **2**, R7 (2000).
[6] J. Mompart and R. Corbalan, Opt. Commun. **156**, 133 (1998).
[7] M. Bajcsy, A. S. Zibrov, and M. D. Lukin, Nature (London) **426**, 638 (2003).
[8] M. Phillips and H. Wang, Phys. Rev. Lett. **89**, 186401 (2002).
[9] A. V. Turukhin, V. S. Sudarshanam, M. S. Shahriar, J. A. Musser, B. S. Ham, and P. R. Hemmer, Phys. Rev. Lett. **88**, 023602 (2001).
[10] Z. S. Yang, N. H. Kwong, R. Binder, and A. L. Smirl, J. Opt. Soc. Am. B **22**, 2144 (2005).
[11] S. Sarkar, P. Palinginis, P. C. Ku, C. J. Chang-Hasnain, N. H. Kwong, R. Binder, and H. Wang, Phys. Rev. B **72**, 035343 (2005).
[12] S. W. Chang, S. L. Chuang, P. C. Ku, C. J. Chang-Hasnain, P. Palinginis, and H. L. Wang, Phys. Rev. B **70**, 235333 (2004).
[13] D. D. Smith, H. Chang, K. A. Fuller, A. T. Rosenberger, and R. W. Boyd, Phys. Rev. A **69**, 063804 (2004).
[14] D. E. Nikonov, A. Imamoglu, and M. O. Scully, Phys. Rev. B **59**, 12212 (1999).
[15] E. S. Fry, X. Li, D. Nikonov, G. G. Padmabandu, M. O. Scully, A. V. Smith, F. K. Tittel, C. Wang, S. R. Wilkinson, and S.-Y. Zhu, Phys. Rev. Lett. **70**, 3235 (1993).
[16] M. Lindberg and R. Binder, Phys. Rev. Lett. **75**, 1403 (1995).
[17] M. E. Donovan, A. Shulzgen, J. Lee, P. A. Blanche, N. Peyghambarian, G. Khitrova, H. M. Gibbs, I. Rumyantsev, N. H. Kwong, R. Takayama, Z. S. Yang, and R. Binder, Phys. Rev. Lett. **87**, 237402 (2001).
[18] M. Phillips and H. Wang, Opt. Lett. **28**, 831 (2003).
[19] L. V. Hau, S. E. Harris, Z. Dutton, and C. H. Behroozi, Nature (London) **397**, 549 (1999).
[20] D. F. Phillips, A. Fleischhauer, A. Mair, R. L. Walsworth, and M. D. Lukin, Phys. Rev. Lett. **86**, 783 (2001).
[21] P. C. Ku, C. J. Chang-Hasnain, and S.-L. Chuang, Electron. Lett. **38**, 1581 (2002).
[22] P. Palinginis, S. Crankshaw, F. Sedgwick, E.-T. Kim, M. Moewe, C. J. Chang-Hasnain, H. Wang, and S.-L. Chuang, Appl. Phys. Lett. **87**, 171102 (2005).
[23] K. Kondo, M. Shinkawa, Y. Hamachi, Y. Saito, Y. Arita, and T. Baba, Phys. Rev. Lett. **110**, 053902 (2013).
[24] C. J. Chang-Hasnain, P. C. Ku, J. Kim, and S.-L. Chuang, Proc. IEEE **91**, 1884 (2003).
[25] W. W. Chow, H. C. Schneider, and M. C. Phillips, Phys. Rev. A **68**, 053802 (2003).
[26] A. A. Belyanin, F. Capasso, V. V. Kocharovsky, Vl. V. Kocharovsky, and M. O. Scully, Phys. Rev. A **63**, 053803 (2001).
[27] J. Houmark, T. R. Nielsen, J. Mørk, and A.-P. Jauho, Phys. Rev. B **79**, 115420 (2009).
[28] P. Lunnemann and J. Mørk, J. Opt. Soc. Am. B **27**, 2654 (2010).
[29] T. R. Nielsen, A. Lavrinenko, and J. Mørk, Appl. Phys. Lett. **94**, 113111 (2009).
[30] D. Barettin, J. Houmark, B. Lassen, M. Willatzen, T. R. Nielsen, J. Mørk, and A.-P. Jauho, Phys. Rev. B **80**, 235304 (2009).
[31] S. Michael, W. W. Chow, and H. C. Schneider, Appl. Phys. Lett. **89**, 181114 (2006).
[32] W. W. Chow, S. Michael, and H. C. Schneider, J. Mod. Opt. **54**, 2413 (2007).
[33] S. Michael, *Theory of Semiconductor Quantum-Dot Systems: Applications to Slow Light and Laser Gain Materials* (Sierke Verlag, Goettingen, 2010).
[34] D. Bimberg, M. Grundmann, and N. N. Ledentsov, *Quantum-Dot Heterostructures* (Wiley, New York, 1998).
[35] V. B. Verma, U. Reddy, N. L. Dias, K. P. Bassett, X. Li, and J. J. Coleman, IEEE J. Quantum Electron. **46**, 1872 (2010).
[36] Q. Zhu, K. F. Karlsson, M. Byszewski, A. Rudra, E. Pelucchi, Z. He, and E. Kapon, Small **5**, 329 (2009).
[37] H. C. Schneider, W. W. Chow, and S. W. Koch, Phys. Rev. B **70**, 235308 (2004).
[38] J. Seebeck, T. R. Nielsen, P. Gartner, and F. Jahnke, Phys. Rev. B **71**, 125327 (2005).
[39] P. Gartner, J. Seebeck, and F. Jahnke, Phys. Rev. B **73**, 115307 (2006).
[40] M. Lorke, T. R. Nielsen, J. Seebeck, P. Gartner, and F. Jahnke, Phys. Rev. B **73**, 085324 (2006).
[41] T. R. Nielsen, P. Gartner, and F. Jahnke, Phys. Rev. B **69**, 235314 (2004).
[42] K. Schuh, P. Gartner, and F. Jahnke, Phys. Rev. B **87**, 035301 (2013).
[43] W. W. Chow and F. Jahnke, Prog. Quantum Electron. **37**, 109 (2013).
[44] H. C. Schneider, W. W. Chow, and S. W. Koch, Phys. Rev. B **64**, 115315 (2001).
[45] S. Hackenbuchner, Ph.D. thesis, Walter Schottky Institute, TU Munich, 2002.
[46] NEXTNANO^3 code, released 24-Aug-2004; see www.nextnano.de/nextnano3/.
[47] S. L. McCall and E. L. Hahn, Phys. Rev. **183**, 457 (1969).
[48] F. A. Hopf and M. O. Scully, Phys. Rev. **179**, 399 (1969).
[49] J. Seebeck, T. R. Nielsen, P. Gartner, and F. Jahnke, Eur. Phys. J. B **49**, 167 (2006).
[50] S. H. Autler and C. H. Townes, Phys. Rev. **100**, 703 (1955).
[51] Z. Deng, D. K. Qing, P. Hemmer, C. H. Raymond Ooi, M. S. Zubairy, and M. O. Scully, Phys. Rev. Lett. **96**, 023602 (2006).
[52] E. Anderson, Z. Bai, C. Bischof, J. Demmel, J. Dongarra, J. Du Croz, A. Greenbaum, S. Hammarling, A. McKenney, S. Ostrouchov, and D. Sorensen, LAPACK *Users' Guide*, 3rd ed. (SIAM, Philadelphia, 1999).